Titre: Title:	Gas-aggregated core–shell ZrN@SiN nanoparticles with enhanced thermal stability for plasmonic applications at high temperatures. Supplément
Auteurs: Authors:	Mariia Protsak, Veronika Cervenkova, Daniil Nikitin, Suren Ali-Ogly, Zdeněk Krtouš, Kateryna Biliak, Pavel Pleskunov, Marco Tosca, Ronaldo Katuta, Hynek Biederman, Bill Baloukas, Ludvik Martinu, Lucia Bajtosova, Miroslav Cieslar, Milan Dopita, & Andrei Choukourov
Date:	2025
Type:	Article de revue / Article
Référence: Citation:	Protsak, M., Cervenkova, V., Nikitin, D., Ali-Ogly, S., Krtouš, Z., Biliak, K., Pleskunov, P., Tosca, M., Katuta, R., Biederman, H., Baloukas, B., Martinu, L., Bajtosova, L., Cieslar, M., Dopita, M., & Choukourov, A. (2025). Gas-aggregated core–shell ZrN@SiN nanoparticles with enhanced thermal stability for plasmonic applications at high temperatures. ACS Applied Nano Materials, 8(6), 3092-3103. https://doi.org/10.1021/acsanm.4c06843

Supporting Information

Gas-Aggregated Core-Shell ZrN@SiN Nanoparticles with Enhanced Thermal Stability for Plasmonic Applications at High Temperatures

Mariia Protsak,*[1] Veronika Červenková,[1,2] Daniil Nikitin,[1] Suren Ali-Ogly,[1] Zdenek Krtous,[1,2] Kateryna Biliak,[1] Pavel Pleskunov,[1] Marco Tosca,[1,3] Ronaldo Katuta,[1] Hynek Biederman,[1] Bill Baloukas,[2] Ludvik Martinu,[2] Lucia Bajtosova,[4] Miroslav Cieslar,[4] Milan Dopita,[5] Andrei Choukourov*[1]

[1] Department of Macromolecular Physics, Faculty of Mathematics and Physics, Charles University, V Holešovičkách 2, 180 00, Prague, Czech Republic

[2]Department of Engineering Physics, Polytechnique Montréal, Montreal, QC H3T 1J4, Canada

[3]ELI Beamlines Facility, the Extreme Light Infrastructure ERIC, Za Radnicí 835, 252 41, Dolní Břežany, Czech Republic

[4]Department of Physics of Materials, Faculty of Mathematics and Physics, Charles University, Ke Karlovu 5, Prague, 121 16, Czech Republic

[5]Department of Condensed Matter Physics, Faculty of Mathematics and Physics, Charles University, Ke Karlovu 5, 121 16, Prague, Czech Republic

*choukourov@kmf.troja.mff.cuni.cz

*mariia.protsak@mff.cuni.cz

Experimental: precleaning of the S_3N_4 targets

It was found that rf sputtering of the Si_3N_4 targets from the 'as is' state produced SiN coatings with poorly reproducible chemical composition and far from stoichiometry. For consistency, we performed pre-sputtering of the Si_3N_4 targets before each experiment. Pre-sputtering was performed at 4 Pa, 3.0 sccm of Ar and 40W rf power. Preliminary tests were performed with different pre-sputtering times, following the elemental content and refractive index of these SiN coatings. It was established that the stoichiometry becomes significantly improved after 30 min of such target conditioning (Table S 1). On the other hand, longer pre-sputtering did not lead to substantial improvement; therefore, it was decided to choose 30 min as a standard protocol.

Table S 1 XPS chemical composition and refractive index of SiN films prepared in the pre-sputtering stage (40 W, Ar 4 Pa, 3.0 sccm).

Sputter time, min	Elemental content, at. %					Refractive index (630 nm)
	C	N	O	Si	Si/N	
10	13.8	14.7	44.1	27.4	1.86	1.56
30	15.2	30.7	23.5	30.5	1.00	1.70

CFD calculations

The combination of the system dimensions and pressure gives a relatively low Knudsen number (Kn < 0.01). This allows for the treatment of the carrier gas flow as a continuum, justifying the solution of carrier gas flow equation using CFD. The following assumptions were made: fluid was treated as an ideal and compressible gas; no slip on the walls was allowed, except for the regions with transitional Knudsen numbers (orifice, deposition chamber), where the Maxwell partial slip model was used; the flow of the fluid was considered laminar. The temperature of the gas in the CFD simulation was set to 21 °C. The simulation accounted for temperature changes due to expansion in the orifice region (Figure S 1). However, we neglected the heating of argon gas by the plasma because the number of hyperthermal species is much smaller than the number of Ar atoms and N_2 molecules.

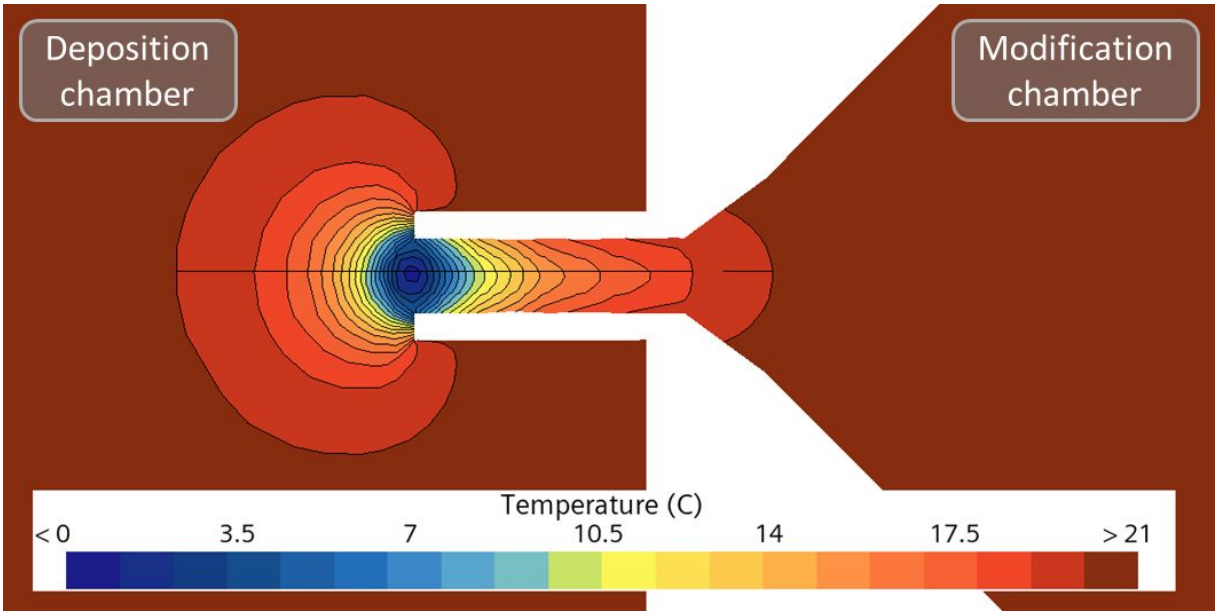

Figure S 1 The temperature gradient over the orifice 2 (Ø7 mm, length 25 mm), between the modification chamber and the deposition chamber. The main temperature is 21 °C, the lowest temperature in the orifice due to expansion is 0.5 °C.

Regarding the pressure drop across the orifice, it can be evaluated from Figure S 2, where a magnified region of orifice 2 is shown. The orifice plays a crucial role in the pressure drop between these chambers. As shown in Table 1 of the main manuscript, the larger the orifice's diameter, the lower the pressure in the modification chamber. This means that a bigger orifice diameter leads to a smaller pressure difference between the deposition and modification chambers.

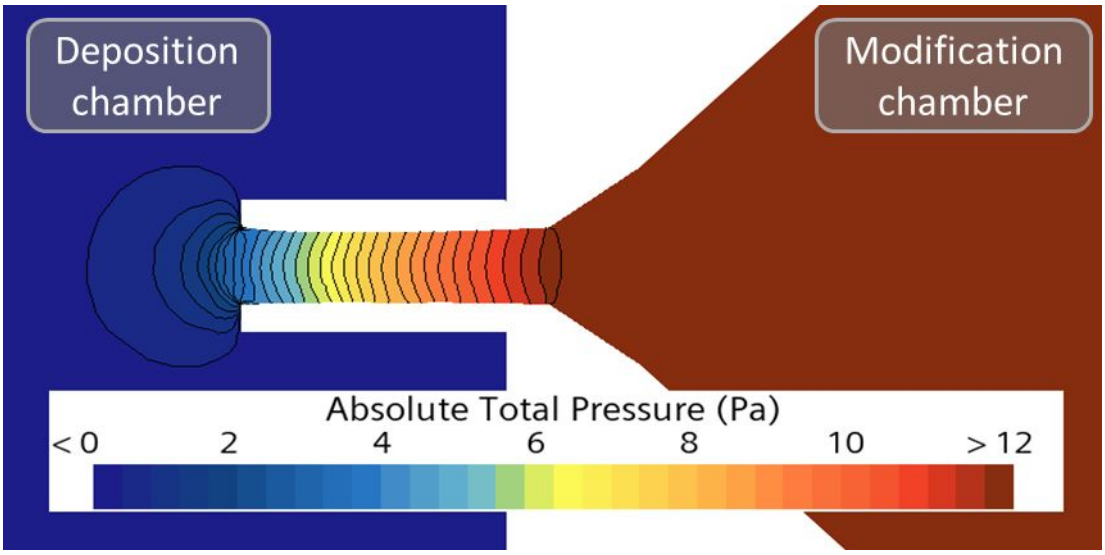

Figure S 2 The pressure gradient over the orifice 2 (Ø7 mm, length 25 mm), between the modification chamber (12.4 Pa) and the deposition chamber (0.1 Pa), resulting in total pressure drop of 12.3 Pa in CFD simulation.

The polyhedral mesh was produced for this simulation. Referring to the mentioned assumptions, it was decided to use steady-state analysis, employing a segregated flow solver with the 2d order convection. SIMPLE pressure-velocity (Semi-Implicit Method for Pressure Linked Equations) coupling algorithm was used to solve Navier-Stokes equations. Afterward, the solved gas flow is 'frozen', i.e. it stores the fluid field data and does not solve the Navier-Stokes equations even if the solver continues to run. In that stage, NPs are then added to the system as solid-state spherical particles and solved transiently (unsteadily), taking the necessary fluid flow information from the previous steady-state simulation. In that case, NPs do not affect fluid flow in any way, but NPs are influenced by the gas flow. The Lagrangian approach is used to describe the evolution of individual particles as they traverse the domain. To cover the NPs behaviour that go through the orifice, an aerodynamic lensing phenomenon was taken into account corrected for the GAS systems as described in ref.[1]

For submicrometric spherical particles moving through the fluid, the drag force can be calculated through the Stokes drag corrected by a Cunningham factor for higher Knudsen numbers.[2,3] In that case, the drag is:[4]

$$\vec{D} = \frac{18 \cdot \mu}{d_p^2 \cdot \rho_p \cdot C_C} \cdot \overrightarrow{v_{ps}} \quad \left[m/s^2\right] \tag{1}$$

Here, μ is the dynamic viscosity of the fluid, d_p is the particle diameter, ρ_p is the particle mass density, $\overrightarrow{v_{ps}} = (\overrightarrow{v_f} - \overrightarrow{v_p})$ is the particle slip velocity (relative fluid velocity over the particle surface), and C_c is the Cunningham correction factor for Stoke's drag:[5]

$$C_C = 1 + \frac{2\lambda}{d_p} \cdot \left(1.257 + 0.4e^{-\left(\frac{1.1 d_p}{2\lambda}\right)}\right) \tag{2}$$

Here, λ is the molecular mean free path from eq. (3):

$$\lambda = \frac{k_B \cdot T_f}{\sqrt{2} \cdot \pi \cdot d_{fm}^2 \cdot p_f} \tag{3}$$

Where, k_B is the Boltzmann constant, T_f is s fluid (gas) temperature, d_{fm} is a fluid molecule or atom diameter (van der Waals diameter is assumed), and p_f is the pressure of the fluid domain. It is important to note that the drag calculated in eq. (1) is the acceleration. To obtain the force, it needs to be multiplied by a particle mass, $\overrightarrow{F_D} = \vec{D} \cdot m_p$.

Considering that the density of ZrN is 7090 kg/m³, we can estimate the mass of the particles. Then, to evaluate the impact of particle size and how gas pressure contributes to drag, we may, for simplicity, consider only the first part of eq. (1) (ignoring slip velocity). For our calculations, we use the following data: Ar gas dynamic viscosity is $\mu = 2.27682 \times 10^{-5}$ Pa·s, gas pressure p_f = 12.4 Pa and 2.5 Pa (7 mm orifice and 15 mm orifice, respectively), van der Waals diameter of Ar atom d_{fm} = 0.2944 nm, gas temperature T_f = 294.15 K = 21 °C. From given input data we can construct Table S 2.

Table S 2 Drag force experienced by ZrN NPs.

Gas pressure [Pa]	**12.4**		**2.5**	
NP size [nm]	**10**	**50**	**10**	**50**
NP mass [kg]	$3.7 \cdot 10^{-18}$	$4.6 \cdot 10^{-16}$	$3.7 \cdot 10^{-18}$	$4.6 \cdot 10^{-16}$
$\frac{\vec{D}}{\overrightarrow{v_{ps}}}$ [1/s]	$2.1 \cdot 10^{2}$	$4.1 \cdot 10^{1}$	$4.1 \cdot 10^{1}$	$8.3 \cdot 10^{0}$

From Table S 2, it can be seen that the mass of a 50 nm nanoparticle is two orders of magnitude higher than that of a 10 nm particle, meaning the 50 nm particle has greater inertia. From the first part of the Cunningham-corrected Stokes drag equation (eq. (1), we see that its value for a 50 nm nanoparticle is an order of magnitude smaller than that for a 10 nm nanoparticle. Consequently, a 50 nm nanoparticle experiences smaller drag, and if the gas pressure is lower (i.e., fewer collisions between NPs and Ar gas molecules), the drag will be reduced further.

Table S 3 XPS chemical composition of ZrN/SiN coatings before and after heating in air.

sample	Temperature, °C	Elemental content, at. %				
		C	N	O	Si	Zr
ZrN	25	31.0	14.1	31.4	-	23.5
	200	21.7	6.7	46.0	-	25.6
	300	15.9	4.6	53.5	-	26.0
	700	13.2	1.8	56.8	-	28.2
ZrN/SiN 40 W	25	16.5	36.3	11.1	33.8	2.3
	200	13.4	33.4	17.7	33.2	2.3
	300	6.1	32.0	25.0	34.4	2.5
	700	2.8	14.6	46.5	32.9	3.2
ZrN/SiN 70 W	25	18.2	36.1	10.5	33.5	1.7
	200	14.5	33.2	16.9	33.7	1.7
	300	7.5	30.8	24.4	35.4	1.9
	700	3.2	17.5	42.2	34.7	2.4
ZrN/SiN 100 W	25	14.9	36.2	13.4	34.1	1.4
	200	11.3	32.9	19.9	34.4	1.5
	300	6.5	31.1	26.1	34.8	1.5
	700	3.3	18.0	42.1	34.8	1.8

The chemical composition of SiN films is characterized by the formula of Si_3N_3O; one N atom is substituted by an O atom in the chemical structure.

Results: size distribution of ZrN@SiN NPs

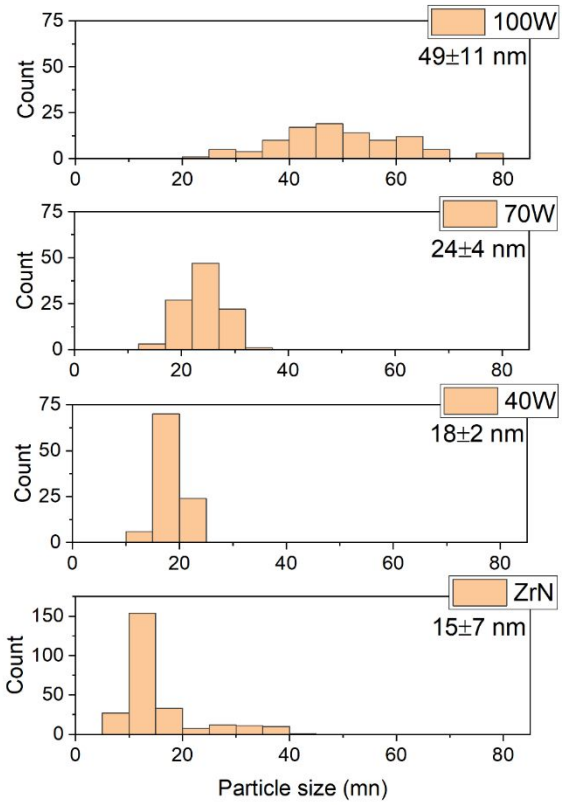

Figure S 3 Size distribution of ZrN NPs and ZrN@SiN NPs prepared at different rf powers on Si_3N_4 magnetron calculated through analysis of TEM images.

Results: gravimetric measurements of density of SiN films

We performed additional depositions to determine the density of SiN films. Using 40 W and 100 W rf power, we deposited 300 nm thick SiN coatings on aluminum foils of 25×75 mm size that were weighed on high-precision balances before and after deposition. With knowledge of deposited volume and mass, we obtained a density of 2.38 g/cm^3 for 40 W and 2.65 g/cm^3 for 100 W. These values are lower than 3.17 g/cm^3 tabulated for bulk Si_3N_4, which also points to the porosity of the coatings.

Results: optical transmission, reflection, and absorptance of quartz substrates

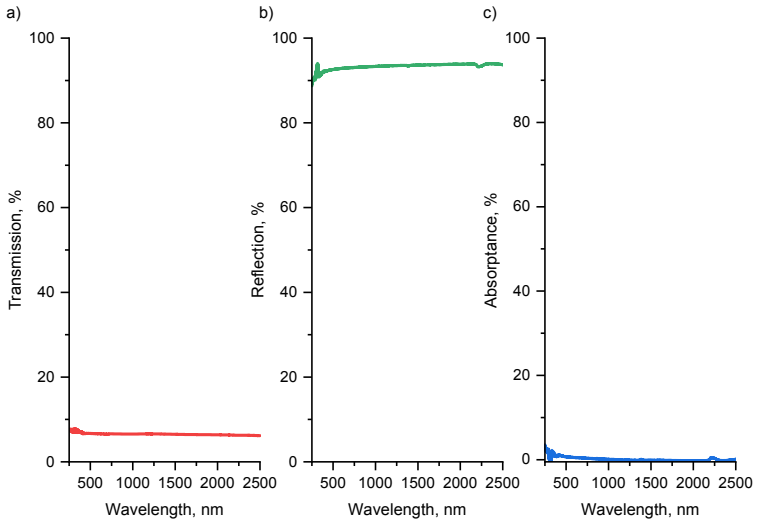

Figure S 4 Optical a) transmission T, b) reflection R, and c) absorptance A of a reference quartz substrate.

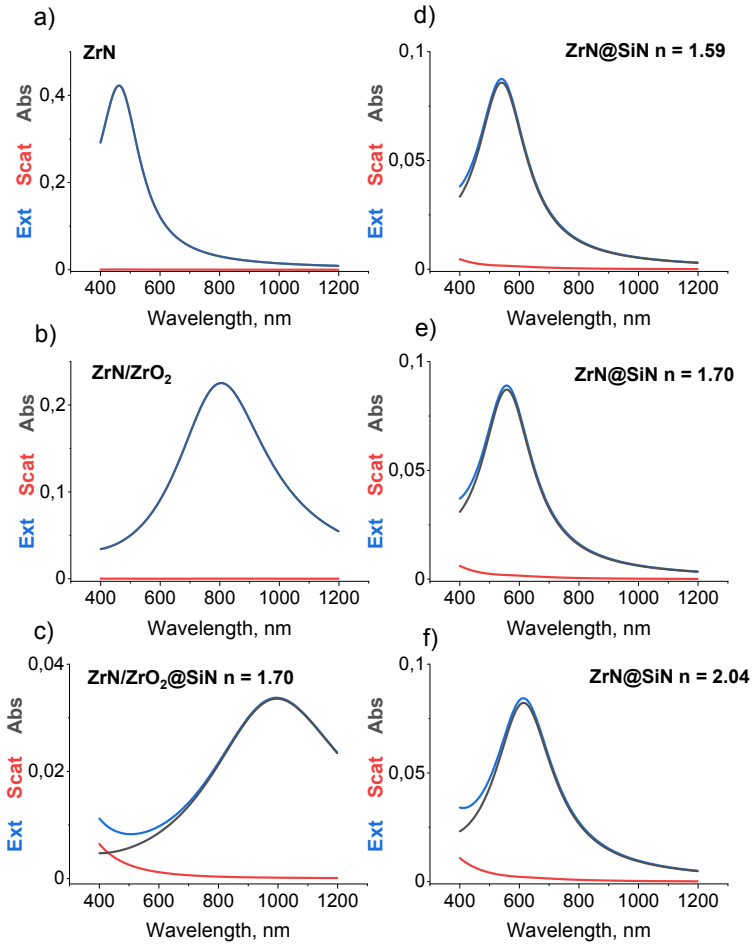

Figure S 5 Calculated optical extinction (Ext), scattering (Scat), and absorption (Abs) spectra: a) stoichiometric ZrN NPs; b) oxidized ZrN NPs approximated by a 30/70 mixture of ZrN and ZrO_2; c) oxidized ZrN NPs with SiN

shell (n_{630} = 1.70); d)-f) stoichiometric ZrN NPs with SiN shells with n_{630} = 1.59, 1.70, and 2.04. The size of the ZrN NPs is 15 nm, and the thickness of the SiN shell is 15 nm.

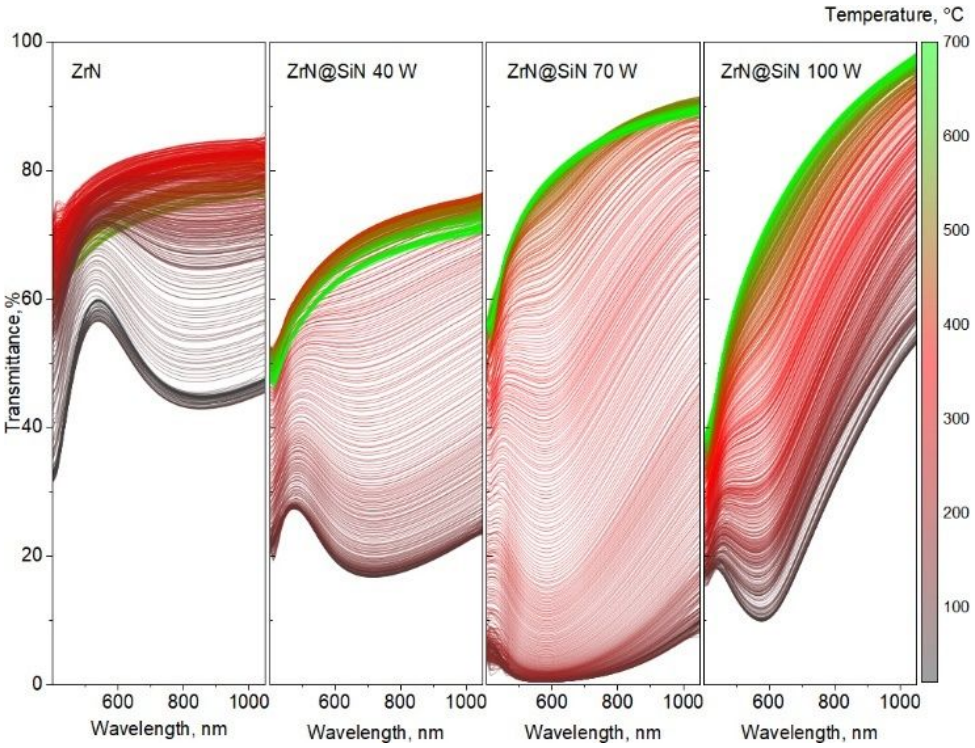

Figure S 6 Optical transmittance of ZrN NPs and ZrN@SiN NPs with shell deposited at different applied powers on the SiN magnetron measured in situ during annealing in air. The samples were deposited on quartz substrates.

For all the samples, the transmittance remains unchanged until a certain temperature is reached, after which it starts to increase in the whole wavelength range. The shape and intensity of the LSPR band are also retained until this temperature, after which the transmittance minimum subsides and eventually disappears. Nevertheless, the crossover temperature differs for different samples.

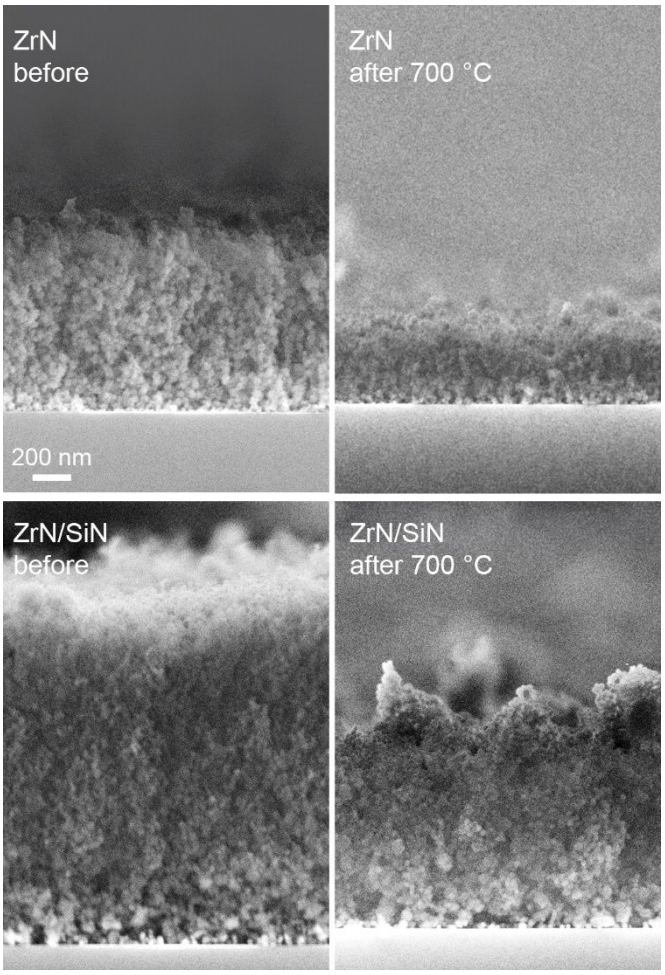

Figure S 7 SEM images of coatings of ZrN and ZrN@SiN (100 W) NPs on Si before and after annealing in air at 700 °C.

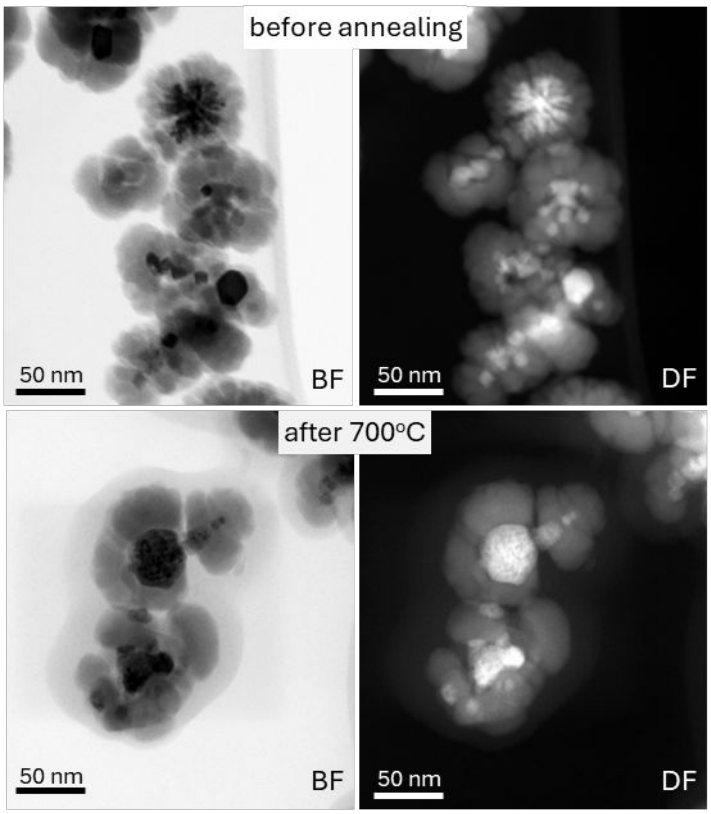

Figure S 8 Bright field and high angle annular dark filed TEM images of ZrN@SiN NPs (100W) measured before and after annealing at 700 °C in air.

References

(1) Kousal, J.; Polonskyi, O.; Kylián, O.; Choukourov, A.; Artemenko, A.; Pešička, J.; Slavínská, D.; Biederman, H. Characterization of Nanoparticle Flow Produced by Gas Aggregation Source. *Vacuum* **2013**, *96*, 32–38. https://doi.org/10.1016/j.vacuum.2013.02.015.

(2) Cunningham, E.; Larmor, J. On the Velocity of Steady Fall of Spherical Particles through Fluid Medium. *Proc. R. Soc. London. Ser. A, Contain. Pap. a Math. Phys. Character* **1910**, *83* (563), 357–365. https://doi.org/10.1098/rspa.1910.0024.

(3) Li, A.; Ahmadi, G. Dispersion and Deposition of Spherical Particles from Point Sources in a Turbulent Channel Flow. *Aerosol Sci. Technol.* **1992**, *16* (4), 209–226. https://doi.org/10.1080/02786829208959550.

(4) Allen, M. D.; Raabe, O. G. Slip Correction Measurements of Spherical Solid Aerosol Particles in an Improved Millikan Apparatus. *Aerosol Sci. Technol.* **1985**, *4* (3), 269–286. https://doi.org/10.1080/02786828508959055.

(5) C N Davies. Definitive Equations for the Fluid Resistance of Spheres. *Proc. Phys. Soc.* **1945**, *57* (4), 259–270. https://doi.org/10.1088/0959-5309/57/4/301.